

Growth, structure and optical characterization of high quality ZnO thin films obtained by spray pyrolysis

F. Paraguay, W. Estrada L., D.R. Acosta N., E. Andrade, M. Miki-Yoshida

Abstract

Zinc oxide thin films were prepared by spray pyrolytic decomposition of zinc acetate onto a glass substrate. Auger spectroscopy showed that the film stoichiometry is close to the ZnO phase with a little excess of oxygen. X-ray diffraction spectra show that the structure belongs to the hexagonal wurtzite crystal type, with a mean crystallite size in the range 20-33 nm. Under optimized deposition conditions films are c-axis oriented, having a full width at half-maximum (FWHM) value of the (002) X-ray diffraction line of 0.238. Microstructure was analysed by scanning electron microscopy (SEM), transmission electron microscopy (TEM), and high resolution electron microscopy (HREM). In regard to the crystal growth, a critical temperature was found to be around 600 K. Above this critical temperature the film is c-axis oriented and almost all grains became round shaped. Optical constants, n and k , were determined using only transmittance data and a direct band gap of 3.28 eV was deduced.

Keywords: Zinc oxide; Spray pyrolysis; Transmission electron microscopy; Scanning electron microscopy.

Introduction

Zinc oxide based coatings are of much interest in science and technology due to their interesting potential applications [1-4], such as in thermoelectric and gas sensor devices, transparent electrodes, selective surfaces, piezoelectric devices, etc. Many

techniques have been employed to produce zinc oxide based coatings [4-8], pulsed laser deposition, reactive sputtering, chemical vapour deposition, spray pyrolysis, etc. Among these techniques, spray pyrolysis has proved to be a simple and inexpensive method, particularly useful for large area applications. However, a conventional spray system usually presents three difficulties: low efficiency (ratio of atoms effectively deposited to those supplied), low deposition rate and rather poor surface uniformity. Improvements in the spray system efficiency have been achieved by the addition of a 'corona spray' to control the transport of aerosol droplets towards the substrate; an efficiency of 80% is reported [9]. Surface roughness depends largely on the size and distribution of the droplets [10]. To achieve a better uniformity in droplet size many alternatives have been proposed. Blandenet et al. [10] used an ultrasonic atomizing system to produce a narrow distribution of droplet size. Viverito et al. [11] worked with a pyrolytic system in which the solution is dispersed to form a fog and, with the aid of a suitable obstruction, larger droplets are returned to be recycled.

In a previous work [12] we described an improved spray system which allowed us to obtain a SnO₂ thin film with high transparency and good surface uniformity. This system improves the selectivity of the droplets that arrive close to the substrate. Then owing to the geometry of the chamber and the gravitational force, the larger droplets cannot be transported by the carrier gas and therefore return to the spray chamber. Using this improved system we have grown undoped zinc oxide thin films and analysed their growing characteristics, atomic composition, surface morphology, microstructure and optical properties. It is important to note that there are many works about thin film microstructure using SEM and X-ray diffraction [13-19] but very little work has been

done using TEM and HREM. To achieve a more complete microstructural characterization we have accomplished TEM and HREM studies.

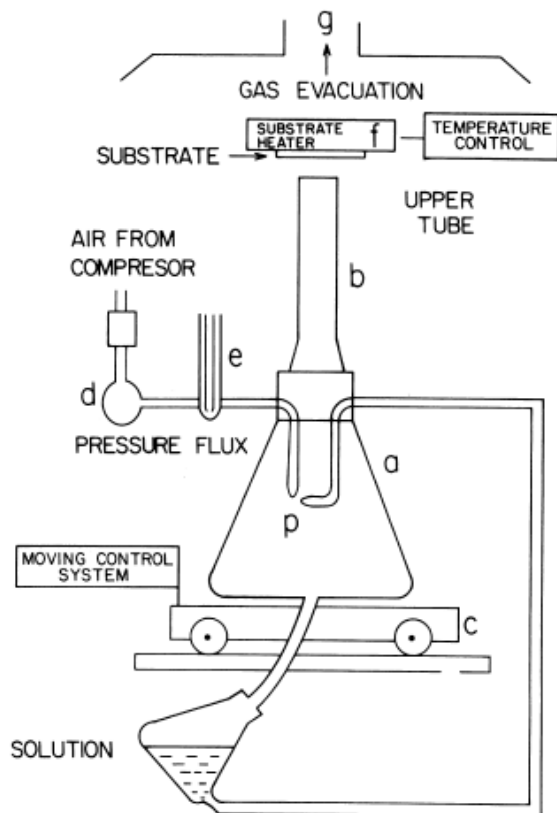


Fig. 1. Schematic representation of the deposition apparatus (from top to bottom): (g), gas evacuation; (f), overhead hot-plate; (b), nozzle; (d), pressure regulator; (e), flowmeter; (a), spraying chamber; (p), glass spray; (c), mobile system.

Experimental:

The main features of the pyrolytic system are fully described elsewhere [12]. For this work some minor changes have been done; the spraying system is illustrated in Fig. 1: an upper tube or nozzle (b) of reduced diameter is used to increase the velocity of droplets in their travel to the reaction zone. In order to produce a uniform film, the spray system was attached onto a mobile stage (c), which provides an oscillatory movement to the spray nozzle set-up. The carrier gas pressure and flux were kept at 310 kPa and

12 l/min respectively. The glass substrate ($2.5 \times 7 \text{ cm}^2$) was attached to the heater (f), their temperature was controlled within $\pm 10 \text{ K}$, and varied between 480 K and 710 K . The concentration of the aqueous solution of zinc acetate was kept within $0.1 \pm 0.4 \text{ M}$, and filtered air was employed as a carrier gas. To enhance the film growth rate we added acetic acid to optimize the solution pH (pH ~ 4 - 4.5) [20]. In order to vary the film thickness, the deposition time was changed among 7 to 25 min. Table 1 summarizes the substrate temperature and thickness of samples analysed in this work.

Zinc acetate dihydrate (ZA) sublimation and decomposition were analysed by mass spectrometry (MS). The ZA sample was heated at 5 K/min between ambient temperature to 720 K . MS spectra were performed in a Thermolab VG gas analyser system. The systems were coupled with a TGA 2950 thermogravimetric analyser for a precise control of the sample temperature. The ZA was initially dried at 375 K for 2 h to remove the water of crystallization. Then the sample was heated at 5 K/min and held constant at 490 K for 30 min . Heating the dried ZA to higher temperatures, above 620 K was used for other experiments. In all the cases the nature of the species obtained and the loss mass rate were recorded. A continuous flow ($50 \text{ cm}^3/\text{min}$) of dry air was introduced as a purge gas.

A profilometer alpha-step and the optical interference method were employed for thickness measurement. Also samples obtained at optimum spray conditions were subjected to depth profile compositional analysis by Auger spectroscopy. This was done using home-made equipment with a cylindrical mirror analyser (CMA) that belongs to INIFTA, Universidad La Plata, Argentina. The coating was sputtered with 2 keV Ar^+

ions. We used Zn (Merck 8778 pro analysis) as standard for calibration and comparison of the spectra.

The microstructure of the films was studied by X-ray diffraction (XRD), scanning electron microscopy (SEM), transmission electron microscopy (TEM) and high resolution electron microscopy (HREM). X-ray diffraction spectra were obtained by a Zeis Jena diffractometer at 30 keV and 20 mA. We used Cu K_a ($\lambda = 1.542 \text{ \AA}$) radiation and the scanning angle 2θ was varied in the range between 30 and 70°. The interplanar distance, lattice parameter, preferential growth orientation and grain size were evaluated from these spectra. Transmission electron micrographs and select area electron diffraction (SAED) patterns were obtained in a CM 200 transmission electron microscope. For these studies the films were peeled off the glass substrate by immersion in HF (~2%) and then they were floated and rinsed in deionized water; finally they were mounted directly on 200 mesh copper grids with carbon supporting [®]Im. Scanning electron micrographs were obtained in a JEM-5800LV scanning electron microscope. Samples were covered with a very thin layer of gold for SEM studies. High resolution electron micrographs were obtained in a top entry JEM-4000FX high resolution electron microscope (HREM), operated at 400 kV, with a point to point resolution of 0.14 nm.

Finally, optical measurements were obtained using a Beckman Lambda 9 spectrophotometer within λ in [300-2500] nm. Optical constants, n and k , were determined by an approximate method using only transmittance data.

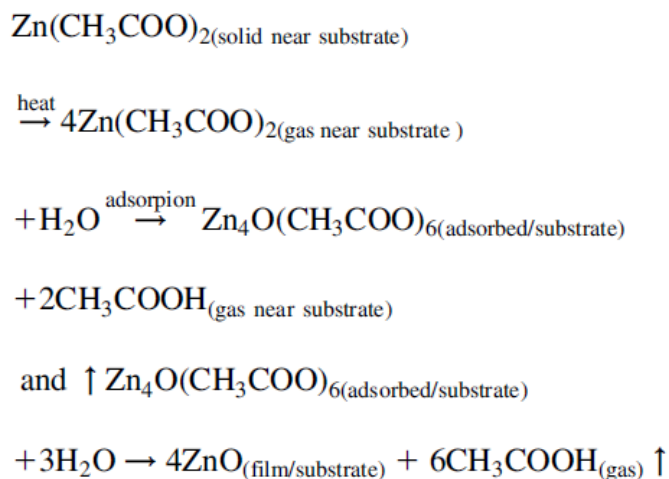
Results and discussion

Table 1

Range of grain size (r), average grain size (a) and dimensions of crystallite aggregates ($b \times l$) (in nm) for samples obtained at different substrate temperatures (T_s). Comparison between values calculated from X-ray diffraction spectra, TEM micrographs and surface grain size observed in SEM micrographs. The thickness (t) of the samples is also tabulated

Sample	T_s (K)	t (nm)	X-ray		TEM			SEM		
			r	a	r	a	$b \times l$	r	a	$b \times l$
Z-808	480	250	21–37	27						30 × 100
Z-822	530	238			6–12	8	30 × 66			40 × 300
Z-007	550	~ 300	18–33	26						
Z-805	570	398	19–32	27						
Z-001	590		23–31	27						
Z-804	600	256			20–48	32	34 × 80	32–120	71	50 × 400
Z-302	650	231	12–24	20						
Z-802	660	170						80–200	120	
Z-308	670	320			16–65	34		50–166	82	
Z-304	690	259	19–29	24	30–140	66		52–243	91	
Z-306	710	162	11–28	22	40–140	83		66–302	96	

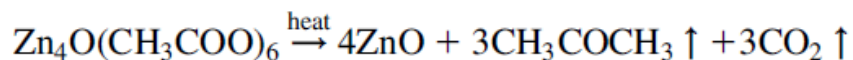
Film growth: Following a similar procedure as discussed in a previous work [12], we found that droplets with radius larger than 55 μm do not reach the substrate. This allowed us to obtain films with good surface uniformity, high optical transmittance and are c-axis orientation. When the aerosol droplets arrive close to the heated substrate a pyrolytic process is produced and a highly adherent film of ZnO develops according to the following steps:



The reaction products must be desorbed out of the surface and then ventilated by the chemical fume hood. Khan et al. [21] proposed that, for ZnO films produced by chemical vapour deposition (CVD), the basic zinc acetate ($\text{Zn}_4\text{O}(\text{CH}_3\text{-COO})_6$ (BZA))

was produced by sublimation of zinc acetate and adsorbed on the substrate; the subsequent pyrolysis of the BZA produces the ZnO film over the substrate surface. Also it has been suggested that the presence of water vapour reduces the amount of residual carbon in the film and could facilitate the final decomposition reaction by the hydrolysis of the BZA [19]. The MS analysis of the sublimation of ZA at atmospheric pressure with dry air as purge gas, in the presence of some residual atmospheric water vapour, only shows the peaks corresponding to the acetic acid. No evidence of other compounds was observed in the ion mass range between 1 and 300 amu. Nevertheless, in the subsequent pyrolysis of ZA, with dry air as purge gas, a clear correlation was observed between the increase of the ion peaks related with the acetone (15, 26, 27, 42, 43 and 58) and carbon dioxide (44) and the decrease of the ZA weight.

These compounds can be associated with BZA decomposition. Fig. 2 shows the principal peaks of the acetone and that corresponding to the carbon dioxide. Also shown are the small peaks corresponding to the acetic acid (45 and 60), that could be produced by the hydrolysis of the BZA with the residual water vapour. This outcome gives unequivocal evidence that also at atmospheric pressure there is formation of BZA and that their pyrolysis occurs between 570 and 620 K by a decarboxylation [19], i.e. by the following reaction:



This result provides unambiguous evidence that the BZA is an important species in the reaction scheme of the spray pyrolysis deposition process; this is the first time that BZA is included in this reaction scheme. However, the presence of H₂O vapour

from the solution may hinder the formation of BZA or could in fact aid its production and its decomposition by a hydrolysis reaction. In all these latter cases there is production of acetic acid. We are still working on this subject.

Fig. 3 shows the deposition rate r as a function of the inverse substrate temperature $1/T_s$. This result was obtained with a 0.1 M aqueous solution of zinc acetate. Two typical regimes can be observed for the deposition rate.

- Zone I ($T_s < 610$ K). In this zone there is a rather linear relationship between the deposition rate (r) and the inverse of the temperature ($1/T_s$). This is typical Arrhenius behaviour in which the deposition rate is limited by the reaction kinetics process at or near the substrate surface [12,22-24] We found an activation energy of 0.59 eV (9.44×10^{-20} J) for this activated region. From microstructural analysis, it is believed that the growth rate is limited by surface diffusion, as discussed below.
- Zone II ($T_s \geq 610$ K). In this region the deposition rate is almost constant, i.e. independent of the temperature. The deposition rate reaches the highest value (1.17 nm/s). It is the typical process in which the growth rate is mass transport controlled [12-15], the reaction kinetics is so fast that the surface reaction finally becomes controlled by mass transfer of the reactants, and the concentration of the reactants on the surface is the limiting parameter.

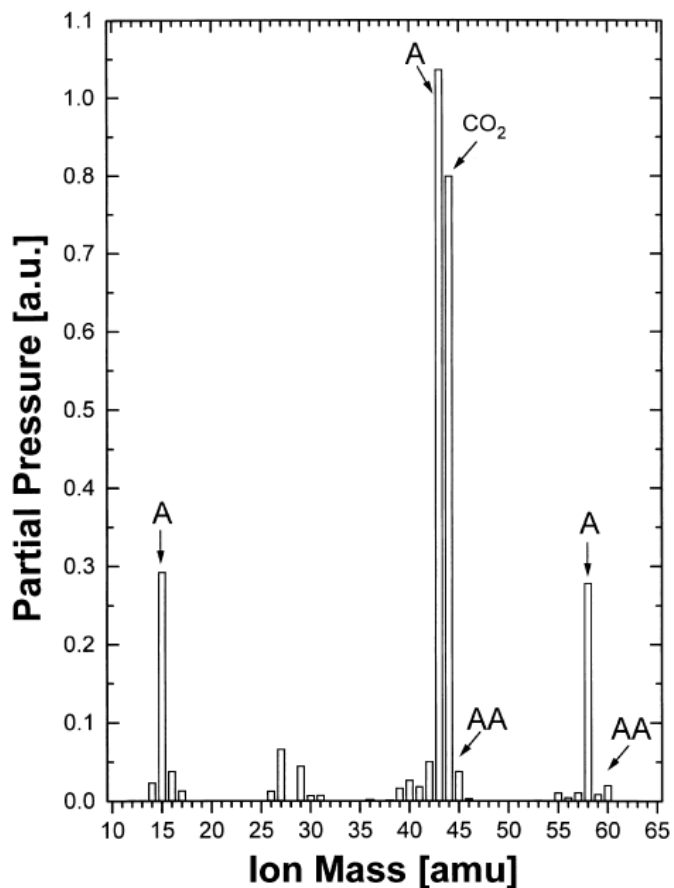


Fig. 2. MS spectrum showing the principal ion peaks of acetone (15, 43 and 58; marked as A) and carbon dioxide (44; marked as CO₂). There are also the small ion peaks corresponding to acetic acid (45 and 60; marked as AA).

The mass flow was estimated as the product of the solution concentration multiplied by the average mist flow rate. We varied the solution concentration between 0.1 and 0.4 M and measured the initial and final volumes of solution to calculate the average mist flow rate. For films obtained at 610 K, we have plotted (Fig. 4) on a log-log scale the deposition rate (r) as a function of the mass flow rate (m). The slope of the straight line obtained by linear leastsquares is approximately unity. Then the deposition rate is proportional to the mass flow; this dependence indicates that the growth is a non-

conventional convective mass transport process, because if this were the case the growth rate should be proportional to $m^{0.5}$ [25].

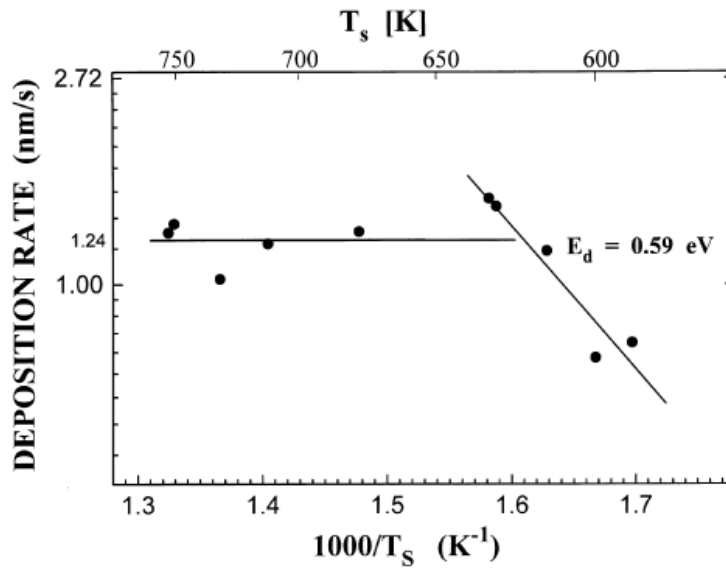


Fig. 3. Semi-logarithmic plot of the deposition rate (r) as a function of the inverse substrate temperature ($1/T_s$).

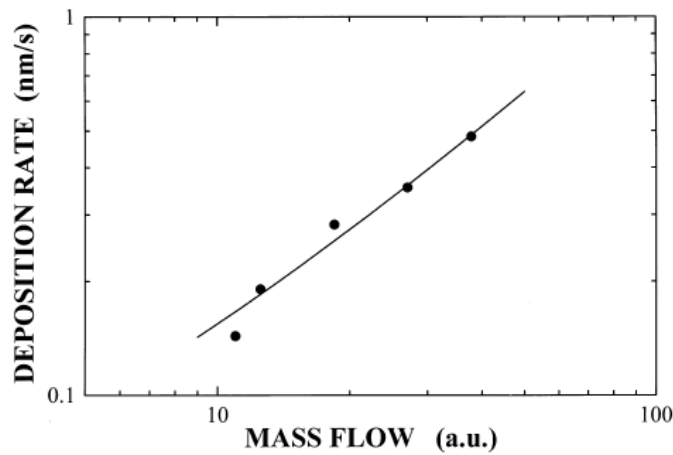


Fig. 4. Log-log plot of the deposition rate (r) as a function of the mass flow rate (m).

Composition:

To obtain the composition depth profile of zinc oxide coatings, a 170 nm thick film (obtained at 610 K) was located in a chamber at 10^{-6} Pa for Auger analysis. Fig. 5 shows Auger spectra with MVV (left peak) and LMM (right peak) Zn transitions, and KLL oxygen transition. In the energy range of the $M_{23}VV$ and $M_{23}M_{45}V$ transitions (Fig. 6) we compared the spectra from pure Zn, pure ZnO and ZnO film over a glass substrate (our sample), obtaining the conclusion that our pyrolytic coatings have the stoichiometry of ZnO. Fig. 7 shows Auger spectra for a sample etched during 0, 90, 210 and 410 min, respectively. The top spectra (without etching) also show the presence of S, Cl and C. When the sample was etched, the peaks of these elements started to decrease, but neither Zn nor O peaks undergo significant variation.

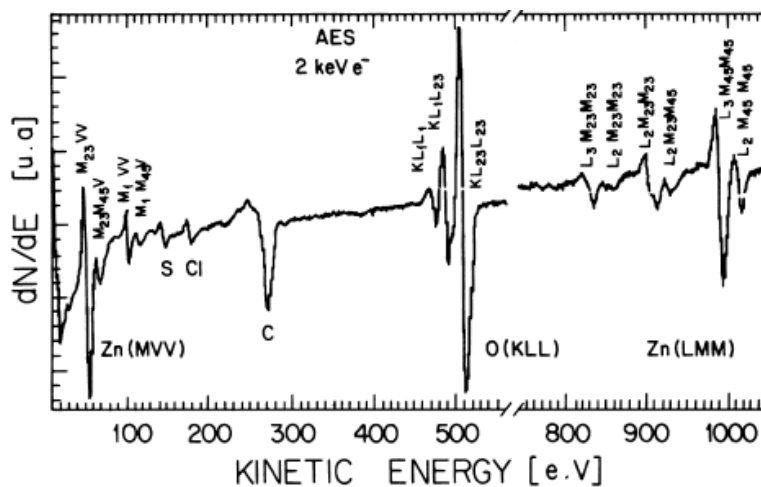


Fig. 5. Auger spectra of ZnO thin film over glass substrate, showing MVV and LMM transitions of the Zn and KLL transition of the oxygen. Small quantities of C, S, and Cl are also shown.

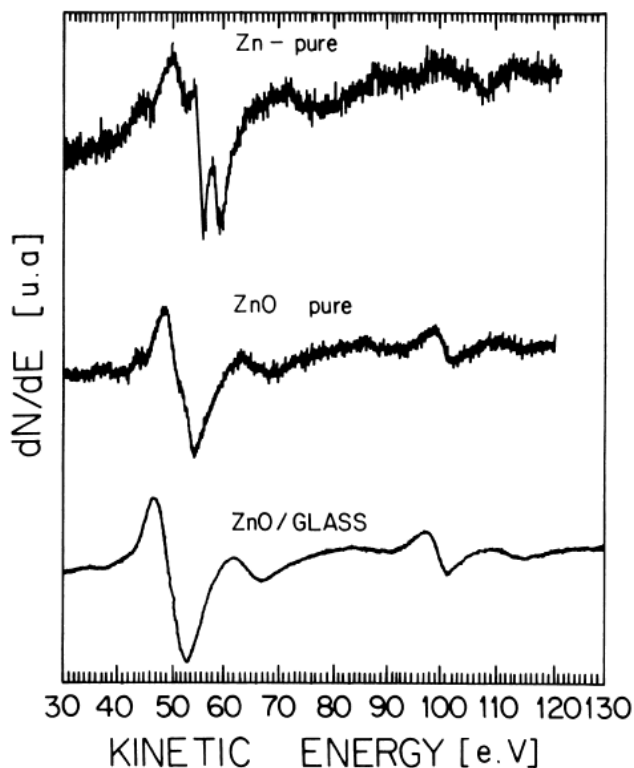


Fig. 6. Comparison of Auger spectra in the range of the transition MVV of Zn, for pure Zn pellet, Zn oxide obtained from oxidation of Zn pellet and zinc oxide thin films samples with spray system.

This result is confirmed in Fig. 8 in which Auger signals are normalized for different sputtering times. These results indicate that the film stoichiometry is close to ZnO and the contamination is only superficial. We can also observe in Fig. 8 that there is a slight reduction of Zn concentration in the outer portion of the ZnO film, in agreement with our Rutherford backscattering spectroscopy (RBS) analysis reported in other work [26], in which some Zn diffusion towards the substrate also was observed.

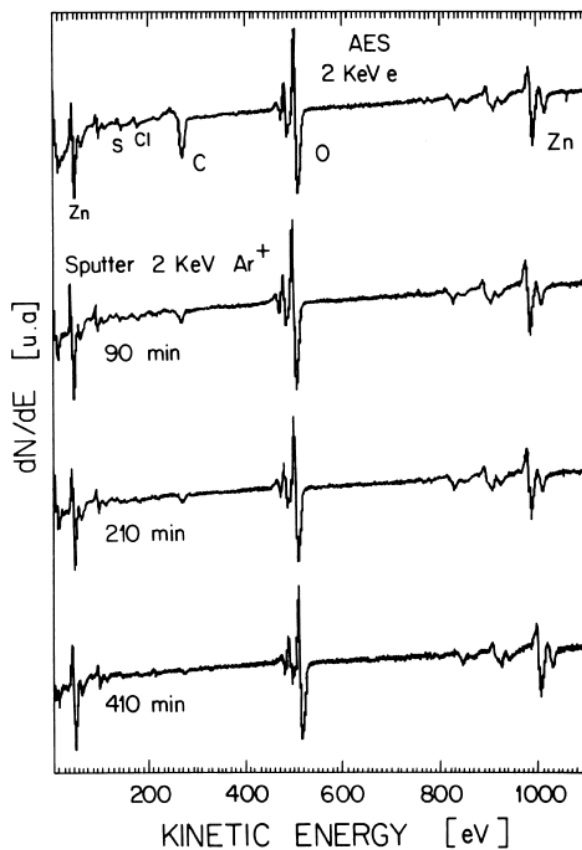


Fig. 7. Auger spectra for a sample etched during 0, 90, 210 and 410 min, showing that the contamination by C, S, and Cl is only superficial.

Structural studies:

Fig. 9 shows the X-ray diffraction spectra for films obtained at 480, 550, 570, 590, 650, 690 and 710 K. The diffraction patterns correspond to hexagonal Wurtzite structure [27]. The preferential growth orientation was determined using the texture coefficient $T_c(hkl)$ [28]. The variation of texture coefficients for (002) and (101) planes with the substrate temperature is shown in Fig. 10. It can be observed that $T_c(002)$ is higher than $T_c(101)$ when the temperature is greater than about 590 K. This means that for deposition temperatures higher than 590 K the film grows preferentially with the (002) plane parallel to the substrate surface, i.e. it is c-axis oriented, with a FWHM between

0.23 and 0.36. This preferential growth can be correlated with TEM and HREM images, as discussed below. Fig. 11 shows the average grain size as a function of the substrate temperature, calculated using the Scherrer formula [29] for planes (100), (002), (101), (102) and (103). From these results it can be concluded that the grain size is almost constant, with a little tendency to decrease with the increase of substrate temperature. Using the same diffraction data we have found that lattice parameters for our samples are: $a = b = 0.3246 \pm 0.0018$ nm, $c = 0.5205 \pm 0.0018$ nm.

SEM secondary electron images of samples Z-808, Z- 822, Z-804 and Z-802 (see Table 1) are shown in Fig. 12. These SEM micrographs show different morphologies of the surface grains, which are dependent on temperature. It is important to emphasize that all these samples have almost the same thickness as can be seen in Table 1. For sample Z- 808 obtained at 480 K (Fig. 12a) the grains are irregular aggregates with characteristic dimension of 100-200 nm length and 25-40 nm width. Fig. 12b shows the surface morphologies of sample Z-822 obtained at 530 K; irregular aggregates can also be observed with characteristic dimension of 100-300 nm. For sample Z-804 prepared at 600 K (Fig. 12c) we observe many bean-like grains with sizes between 200 and 400 nm in length and 50-100 nm wide. Also many smaller round grains of about 100 nm are shown. Fig. 12d shows a SEM micrograph of sample Z-Z-802 obtained at 660 K. An evident change in grain morphologies can be observed; almost all grains became round shaped of about 80-200 nm in size. These changes in the grain morphologies can be correlated with the changes of growth rate control mechanism. It was pointed out that samples prepared below 610 K grow with the deposition rate limited by the reaction kinetics process at or near the substrate surface;

this process gives rise to films with irregular or edge-like grains (Fig. 12a,b). Whereas for films obtained at or above 610 K the growth rate is mass transport controlled; this mechanism gives rise to almost round shaped grains (Fig. 12d). Finally, it can be presumed that the microstructure of bean-like grains could be a transitional one between irregular and round grains (Fig. 12c).

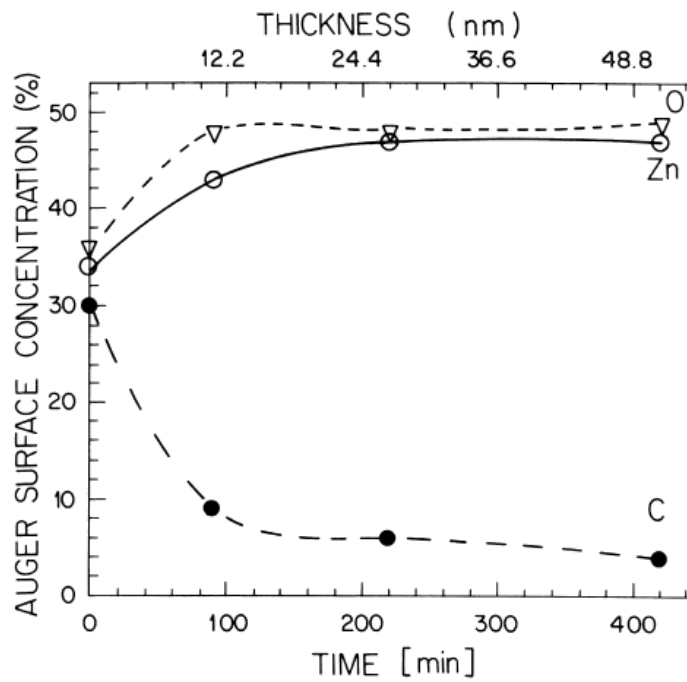


Fig. 8. Auger signals are normalized for different sputtering times. It can be concluded that the film stoichiometry is close to ideal ZnO.

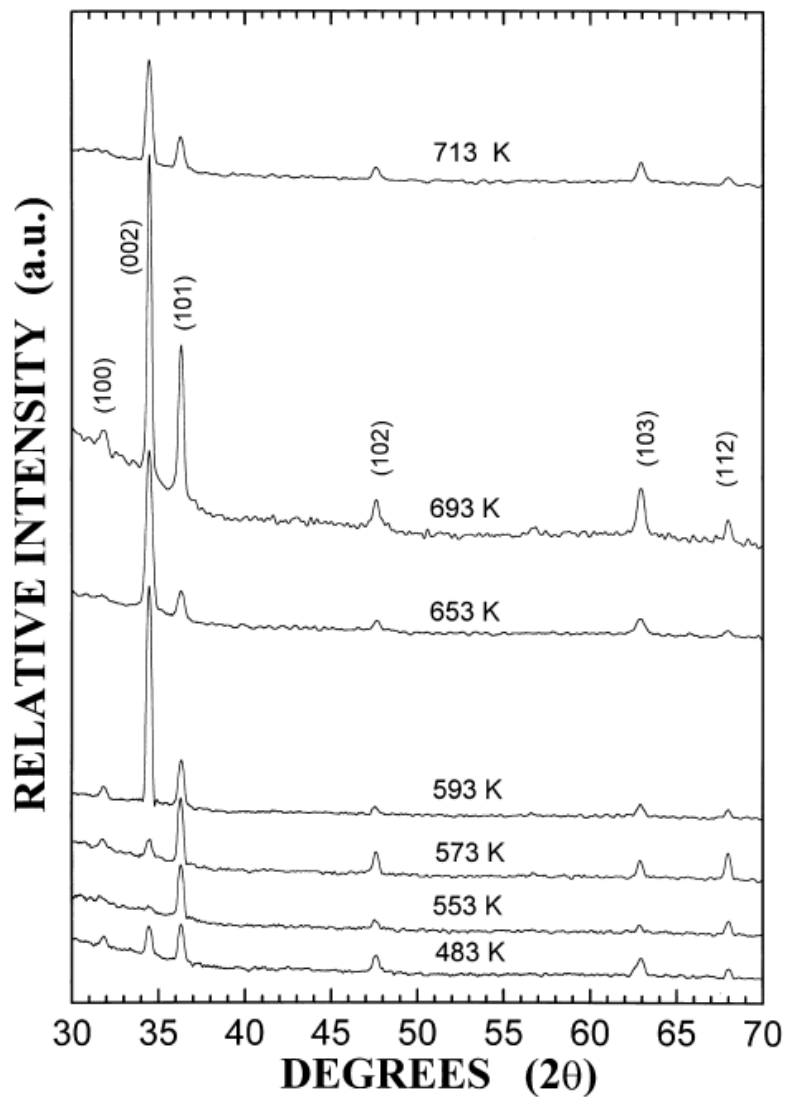


Fig. 9. X-ray diffraction spectra for films obtained at 480, 550, 570, 590, 650, 690 and 710 K. It clearly shows the change of preferential growth orientation at about 590 K.

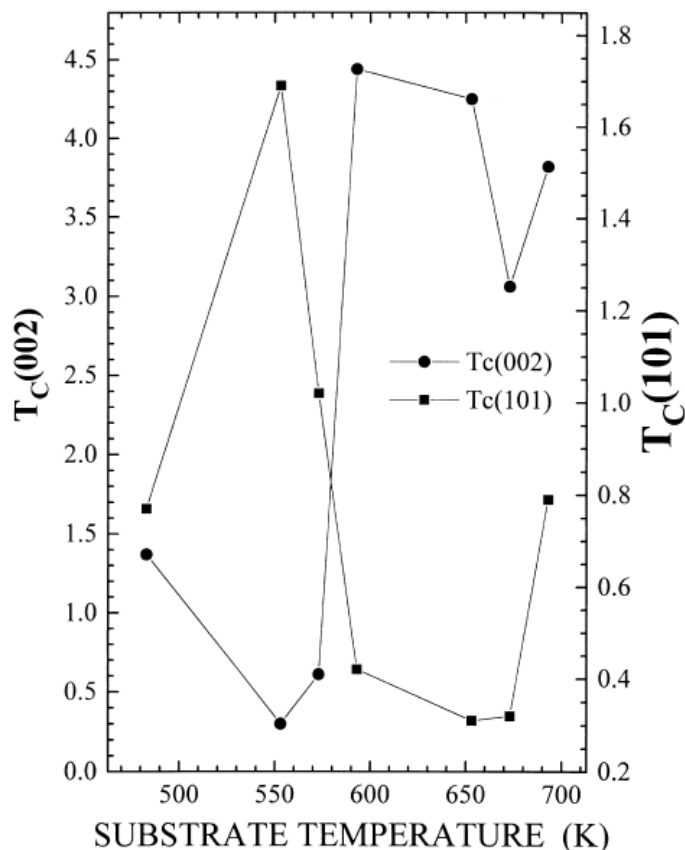


Fig. 10. Variation of texture coefficients for (002) and (101) planes with the substrate temperature.

Bright field TEM micrographs and their corresponding SAED patterns of samples Z-822, Z-804 and Z-308 (see Table 1) are shown in Fig. 13. TEM images show that grains are formed by many small crystallite aggregates with sizes varying between 6 and 12 nm. These small crystallites cannot be clearly observed in SEM images and this is the reason for the discrepancy between the grain size obtained by X-ray diffraction and that observed in SEM images [13-17]. By X-ray diffraction we calculate the mean dimension of the crystallites perpendicular to the diffracting plane whereas in SEM images we observe the aggregates. Fig. 13a shows the microstructure of sample Z-822, clearly showing the aggregates of crystallites.

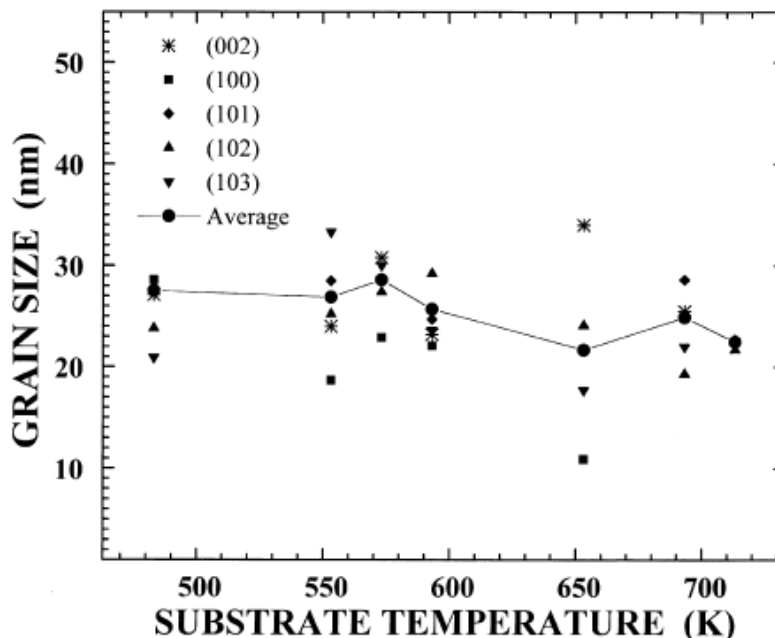


Fig. 11. Average grain size calculated using the Scherrer formula for planes (100), (002), (101), (102) and (103).

Also in many grains it can be seen that the crystallites are ordered in a layered-like structure (marked LS), in which each one layer would correspond to aggregates of crystallites with the basal plane (002) parallel to the layer. In this case the layers do not correspond with the orientation of the substrate surface, as is expected with the preferential growth orientation of this sample. The corresponding SAED pattern shown in the inset of Fig. 13a presents the rings, ascribed to the (100), (002) and (101) planes, shaped by many strong spots. This confirms the fact that many crystallites do not have their basal planes normal to the electron beam, i.e. they are inclined with respect to the substrate surface. This affirmation is also supported by HREM micrographs (see Fig. 14a). The micrograph of sample Z-804 and the corresponding SAED pattern in the inset, are shown in Fig. 13b. A microstructure of layered-like aggregates of crystallites, resembling that of the sample Z-822, is seen. However, now the sample, obtained at

600 K, has the (002) plane as the preferred growth orientation; also it can be observed that the layers became nearly normal to the electron beam (marked L), i.e. parallel to the substrate surface. The SAED pattern shows the rings corresponding to the planes (100), (002) and (101). In the present case the (002) ring shows a small number of very weak spots indicating that only some of the crystallites have their (002) planes in diffraction condition, i.e. nearly parallel to the electron beam. This fact is congruent with X-ray diffraction results. Fig. 13c shows the micrograph of sample Z-308, obtained at 670 K, and the corresponding SAED pattern. A more densely packed aggregate of crystallites can be seen, and again the layered-like structure parallel to the substrate surface can be observed. In this sample the crystallites are less visible, perhaps due to the crystallite coalescence at this high temperature. Also in this case the SAED pattern shows the (002) ring with a limited number of very weak spots, as expected from the fact that the (002) plane is the preferred growth orientation. In all these SAED patterns we have marked with an arrow the (002) spots between the (100) and (101) rings. The d-spacings have been accurately determined from the SAED patterns and tabulated in Table 2; they are also compared with those of reference [27].

Furthermore, in the spray pyrolysis deposition of thin films, several factors are involved that make it different from sputtering or evaporation of thick films: (a) the kinetic energy of reactants in the spray system is very low ($\sim 10^{-1}$ eV); (b) the ambient gas pressure is higher (atmospheric); (c) the deposition rate is generally lower (~ 1 nm/s); (d) the film thickness is smaller (~ 200 - 300 nm). Nevertheless some similitude can be noticed in the different microstructures observed in our films and those described in the growth model of Thornton [30,31] for sputtered thick films. It can be pointed out that our

films, were obtained at T_s/T_m between 0.2 and 0.3 (T_s substrate temperature and T_m film-material melting temperature). For low substrate temperatures (T_s , 500 K), the films have microstructures similar to that of the zone 1, i.e. formed of many tapered crystallites with domed tops. This morphology can be due to the fact that ambient gas, at atmospheric pressure, reduces the surface mobility of reactants. Then the initial nuclei tend to grow in the direction of available reactant flux, giving rise to a very rough surface, with many edge-like grains, as can be seen in Fig. 12a. However, the relatively low deposition rate inhibits the formation of a voided structure, as reported for sputtered film [30]. Also this growth zone persists to higher T_s/T_m at high ambient pressures, probably due to the fact that adsorbed ambient atoms limit the reactants mobility.

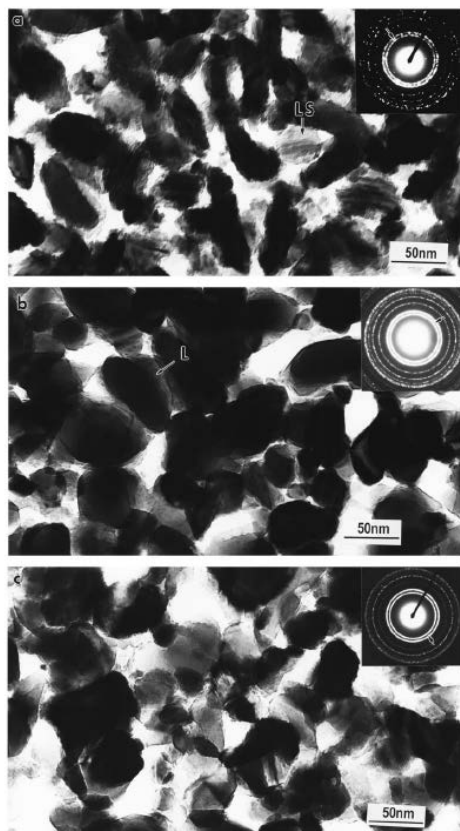


Fig. 13. Bright field TEM micrographs, and their corresponding SAED patterns in the inset, of samples (a) Z-822, (b) Z-804 and (c) Z-802.

Fig. 14a shows HREM micrographs of sample Z-804. In Fig. 14a it can be clearly observed that a grain, of about 30-35 nm in size, is really an aggregate of many small crystallites of around 6-10 nm. Some crystallites (marked HC) of hexagonal shape can also be seen, the high resolution spots observed in this crystallite corresponding to columns of atoms located in (100) and (011) planes, as deduced from interplanar distances and angles. Fig. 14b shows a HREM micrograph of the typical grain boundary observed in our samples. It is interesting to notice that some amorphous material surrounds the grains and the extent of this boundary region could be correlated with the depleted zone of the conduction model [32,33] of ZnO thin films.

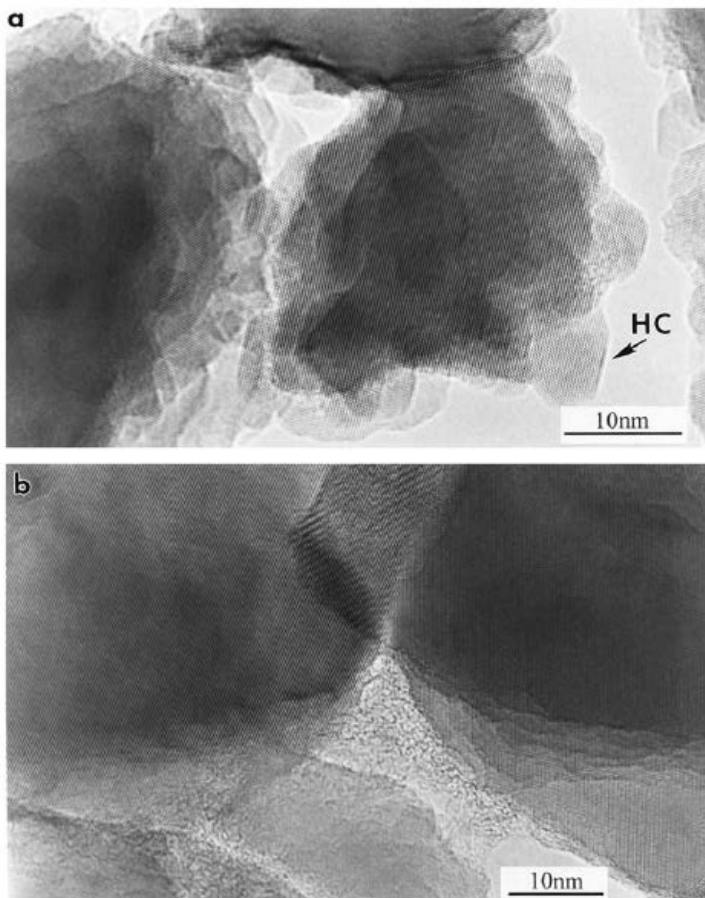


Fig. 14. HREM micrographs of sample Z-804. (a) A grain, of about 30–35 nm in size, is really an aggregate of many small crystallites of around 6–10 nm. (b) Typical grain boundary observed in our samples.

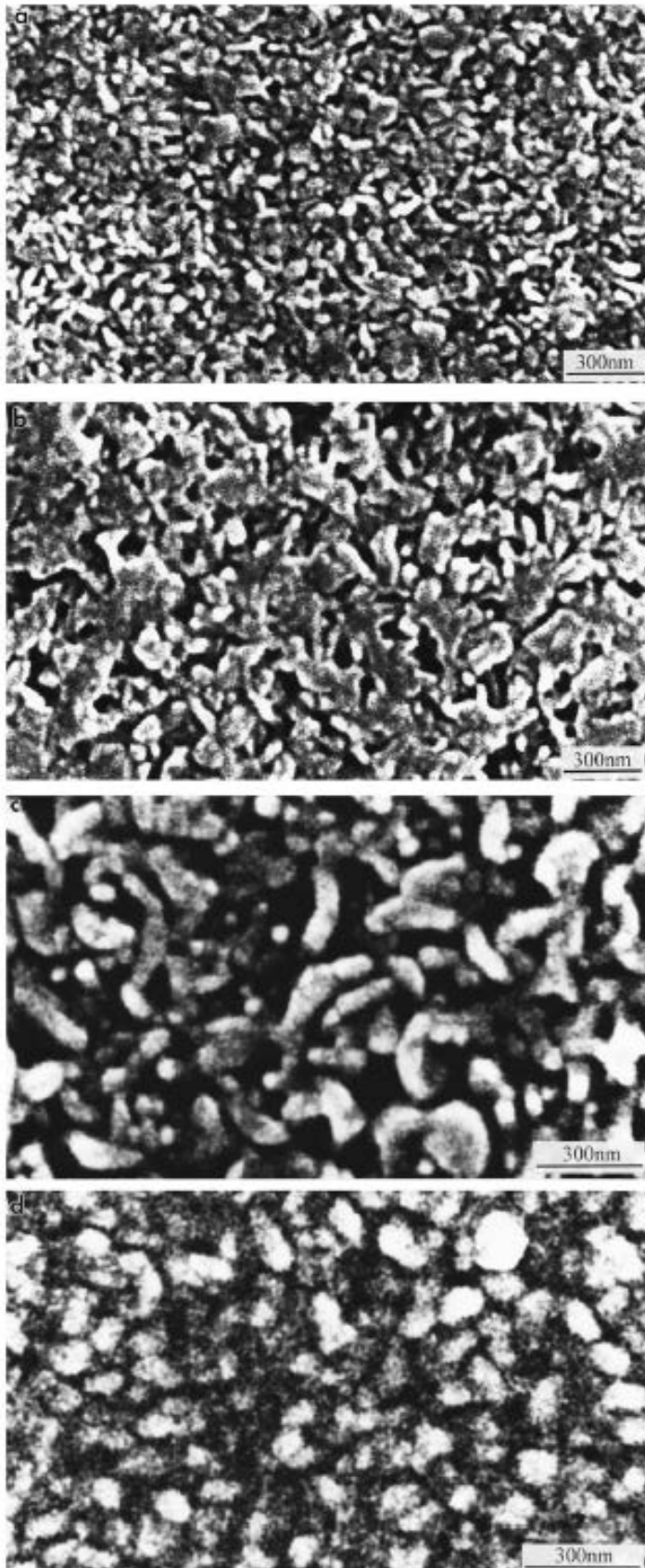


Fig. 12. SEM secondary electron micrographs for films obtained at (a) 480 K (sample Z-808), (b) 530 K (sample Z-822), (c) 600 K (sample Z-804), and (d) 670 K (sample Z-802). See text for details.

Optical properties: Fig. 15 shows the spectral transmittance (T_λ) and reflectance (R_λ) at near normal incidence for the sample Z-007 obtained at 550 K (see Table 1). It can be noticed that the film has a high optical transmittance, higher than 85%, and also it has an optical absorptance almost zero in the visible range ($T_\lambda + R_\lambda \sim 1$). A simple and reliable method was employed to obtain the refractive index (n) in the visible region. Considering the absorptance of nearly zero in the wavelength range between 400 and 800 nm, then the optical transmittance, for normal incidence, is given by [34]

$$T(\lambda) = \frac{8n_0n^2n_2}{(n^2 + n_2^2)(n^2 + n_0^2) + 4n_0n^2n_2 - (n^2 - n_2^2)(n^2 - n_0^2)\cos(4\pi nd/\lambda)}$$

(1)

where $n_0 = 1.55$ is the substrate refractive index, n is the

where $n_0 = 1.55$ is the substrate refractive index, n is the film refractive index, n_2 is the refractive index of air, l is the wavelength, and d is the film thickness.

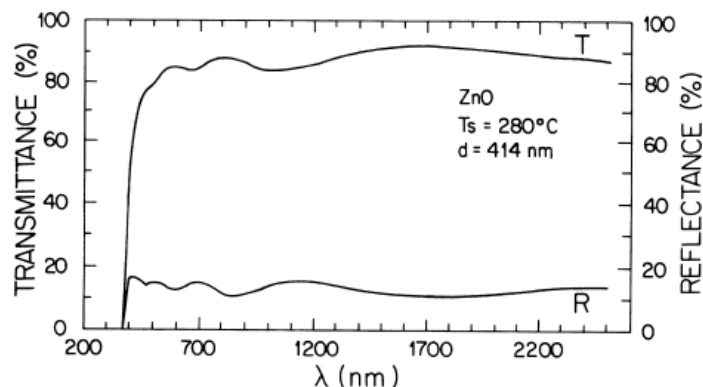


Fig. 15. Spectral transmittance (T) and reflectance (R) at near normal incidence for a 414 nm thick ZnO sample.

Table 2
Interplanar distance, for samples obtained at different temperatures, calculated from the SAED patterns, compared with the ZnO card (36-1451) of JCPDS

(hkl)	JCPDS	Z-808, 480 K	Z-822, 530 K	Z-804, 600 K	Z-302, 650 K	Z-308, 670 K	Z-304, 690 K	Z-306, 710 K
100	0.281	0.280	0.281	0.280	0.281	0.282	0.280	0.284
002	0.260	0.259	0.260	0.261	0.263		0.261	
101	0.248	0.245	0.245		0.249	0.248	0.245	0.248
102	0.191	0.189	0.190	0.191	0.192	0.189	0.190	0.193
110	0.163	0.161	0.162	0.162	0.163	0.164	0.161	0.163
103	0.148	0.147	0.147	0.147	0.149	0.150	0.147	
200	0.141	0.140	0.144	0.141	0.141	0.140	0.140	0.141
112	0.138	0.137	0.135	0.137	0.139		0.138	0.137
201	0.136	0.135		0.136		0.136	0.135	
004	0.130							
202	0.124	0.123	0.123	0.123			0.123	
104	0.119	0.108	0.115	0.117				
203	0.109	0.105		0.109	0.109	0.109	0.108	
210	0.106	0.103		0.106	0.106		0.105	
211	0.104		0.103	0.103	0.104	0.104	0.103	

From Eq. (1), the minimum values of the transmittance, T_m , in the spectrum can be found:

$$T_m(\lambda_m) = \frac{4n_0n^2n_2}{(n_0n_2 + n^2)^2} \quad (2)$$

Starting at this equation we can calculate n , knowing T_m , n_2 and n_0 . In order to obtain the values of n for different wavelength, we fabricated samples under the same spray conditions, only varying the deposition time to obtain different thicknesses. Fig. 16 gives the n values for different wavelengths in the visible range; it is almost constant giving $n = 1.88 \pm 0.04$. Otherwise in the wavelength range 365-400 nm the absorption is quite significant, therefore transmittance can be approximated by:

$$T(\lambda) = Ae^{-\alpha(\lambda)d} \quad (3)$$

$$A = \frac{16n_0(n^2 + k^2)}{[(n + n_0)^2 + k^2][(n + n_2)^2 + k^2]}$$

Where a is the absorption coefficient. Both α and A are

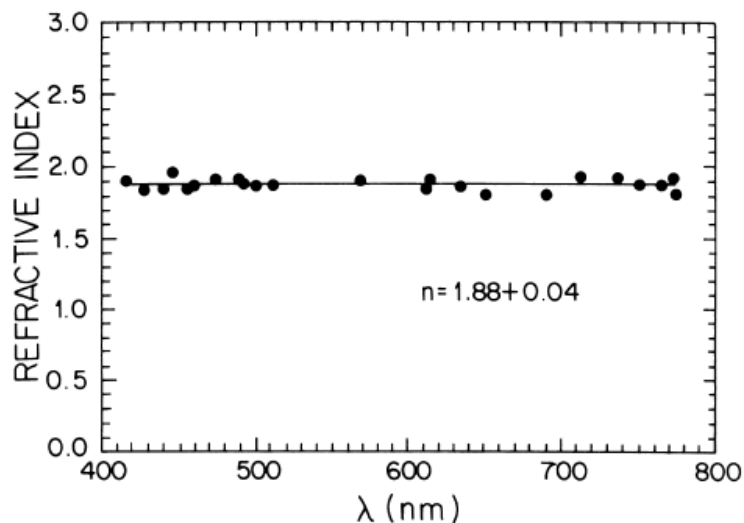


Fig. 16. Refraction index (n) values calculated from transmittance spectra in the high transmittance range (400–800 nm).

parameters that depend on wavelength. To obtain the $a(\lambda)$ values, we use the same transmittance spectra T for different thickness and we need to obtain for each wavelength λ_i the slope of the plot $\ln(T(\lambda_i))$ versus d . The linearity between $\ln(T)$ and d means that A is almost constant for the range analysed. The extinction coefficient (k) can be calculated from the values of a ; also with the intercept ($d = 0$) of the plot we obtain $\ln(A)$. Using Eq. (3) for A , we determine n using the calculated values of k and the intercept $\ln(A)$. The spectral values for k and n are given in Fig. 17. To resolve whether the material has a direct or indirect band gap, plots of $(\alpha E)^2$ versus E and $(\alpha E)^{1/2}$ versus E were analysed. Better linearity was observed in the former case (see Fig. 18), from which the optical energy gap is obtained by extrapolating the linear portion of the absorption spectrum to $\alpha E = 0$. Thus, an energy gap of $E_g = 3.28$ eV was deduced. This value is somewhat smaller than the bulk value of 3.31 eV for ZnO [35]. Therefore for our pyrolytic ZnO films the predominance of a direct transition is concluded, in agreement with other results in the literature [35,36]. Fig. 18 also shows

the low energy Tauc tail, which can be ascribed to defects and impurities [37]. The extremely high electrical resistance, in the order of tens of MV, observed for our ZnO coatings can be attributed to

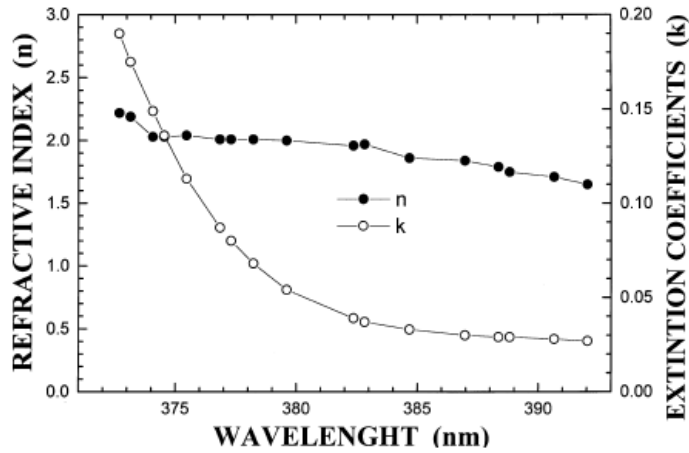


Fig. 17. Calculated extinction coefficient (k) and refraction index (n) for the high absorption range (< 400 nm).

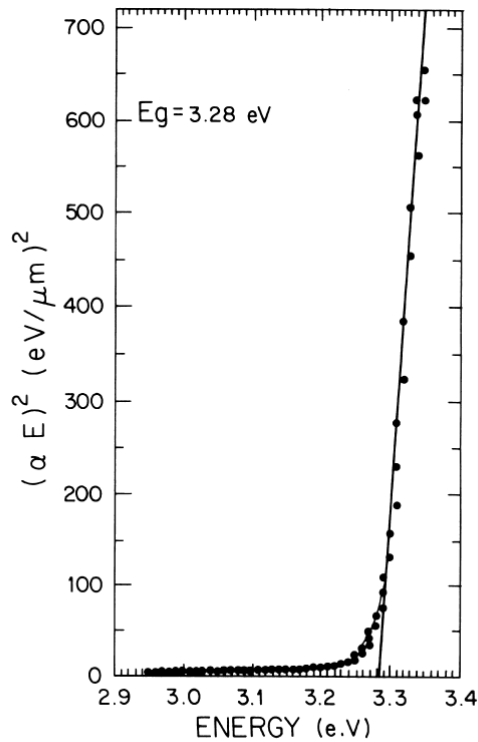


Fig. 18. Plots of $(\alpha E)^2$ as a function of the energy (E), from which an optical energy gap of $E_g = 3.28$ eV was deduced.

the large density of extrinsic traps at the grain boundaries due to oxygen chemisorption. These traps deplete the grains and result in a charge carrier barrier at the grain boundary [37]. This effect can be more relevant for small grain size, therefore the deposition technique plays a fundamental role in the electrical and optical properties. This supposition is in agreement with the fact that electrical resistance drops two orders of magnitude when the ZnO is inside a high vacuum chamber, which allowed us to perform the Auger analysis without a conductive layer. This effect can also be pertinent for gas detection devices.

Conclusions

The spray system used in this work gave rise to a good size selectivity of droplets which allowed us to obtain uniform high quality ZnO films. It means that they have high optical transmittance, higher than 85%, and they are c-axis oriented with the FWHM of the (002) X-ray reflection line being as low as 0.238. The surface morphology and microstructural characteristics of the films are highly dependent on deposition temperature. A critical temperature was found to be around 600 K; over which the individual crystals grow preferentially with their crystallographic c-axis perpendicular to the substrate, with the film structure formed by more or less compact layers of crystallite aggregates (marked L in Fig. 13b). Also above this temperature the growth control mechanism became mass transport. Below this critical temperature the films do not have a preferential growth direction and their microstructure is more porous with layers of crystallite aggregates inclined with respect to the substrate surface. The films have a direct band gap, with an optical value of 3.28 eV.

Acknowledgements

The authors would like to thank the International Program for Physical Sciences (IPPS) for financial support. They wish to express their appreciation to Dr J.M. Heras and G. Benites from INIFTA-Argentina for Auger spectra and to J.C. Pineda, A. Reyes, D. Lardizabal and R. Guerrero for assistance with the experimental work. Also this work was partially supported by a grant from CONACyT N8 211302- 5-4559A.

References

- [1] M.G. Ambia, M.N. Islam, M. Obaidul, Hakim, J. Mater. Sci. 27 (1992) 5169.
- [2] A.P. Roth, D.F. Williams, J. Appl. Phys. 52 (1981) 6685.
- [3] S. Major, S. Kumar, M. Bhatnagar, K.L. Chopra, Appl. Phys. Lett. 49 (1986) 394.
- [4] Z.C. Jin, I. Hamberg, C.G. Granqvist, J. Appl. Phys. 64 (1988) 5117.
- [5] V. Craciun, et al., Phys. Lett. 65 (23) (1994) 2963.
- [6] S.K. Ghandi, R.J. Field, J.R. Shelly, Appl. Phys. Lett. 37 (1980) 449.
- [7] A.F. Aktaruzzaman, G.L. Sharma, L.K. Malhotra, Thin Solid Films 198 (1991) 67.
- [8] M. de la L. Olvera, et al., Thin Solid Films. 229 (1993) 196.
- [9] W. Siefert, Thin Solid Films 121 (1984) 267.
- [10] G. Blandenet, M. Court, Y. Lagarde, Thin Solid Films 77 (1981) 81.
- [11] T.R. Viverito, E.W. Rilee, L.H Slack, Am. Ceram. Soc. Bull. 54 (1975) 217.
- [12] M. Miki-Yoshida, E. Andrade, Thin Solid Films 224 (1993) 87.
- [13] H. GoÂmez, et al., Thin Solid Films. 293 (1997) 117.

- [14] C. Messaoudi, D. Sayah, M. Abd-Lefdil, Phys. Stat. Solidi A 151 (1995) 93.
- [15] K. Kobayashi, et al., Thin Solid Films 266 (1995) 106.
- [16] J.L. Deschanvres, B. Bochu, J.C. Joubert, J. Phys. III France 4 (1994) 1243.
- [17] J. Hu, R.G. Gordon, J. Appl. Phys. 71 (2) (1992) 880.
- [18] J.L. van Heerden, R. Swanepoel, Thin Solid Films. 299 (1997) 72.
- [19] G.L. Mar, P.Y. Timbrell, R.N. Lamb, Chem. Mater. (1995) 7.
- [20] F. Caillaud, A. Smith, J.F. Baumard, J. Am. Ceram. Soc. 76 (4) (1993) 998.
- [21] O.F.Z. Khan, P. O'Brien, Thin Solid Films 173 (1989) 95. A.K. Gyani, O.F.Z. Khan, P. O'Brien, D.S. Urch, Thin Solid Films 182 (1989) L1.
- [22] J. Sanz Maudez, T. Rodriguez, Thin Solid Films 69 (1980) 183.
- [23] F. Caillaud, A. Smith, J.F. Baumard, Thin Solid Films 208 (1992) 4.
- [24] V. Vasu, S. Subrahmanyam, Thin Solid Films 189 (1990) 217.
- [25] J.A. Dirksen, T.A. Ring, Chem. Eng. Sci. 46 (10) (1991) 2389.
- [26] F. Paraguay, MSC Thesis, Universidad Nacional de Ingenieria, 1997.
- [27] Joint Committee on Powder Diffraction Standards, Powder Diffraction File, International Center for Diffraction Data, Swarthmore, PA, 1988, card 36-1451.
- [28] C.S. Barret, T.B. Massalski, Structure of Metals, Chapter 9, Pergamon Press, Oxford, 1980.

<https://cimav.repositorioinstitucional.mx/jspui/>

[29] E.F. Kaelble (Ed.), Handbook of X-rays, Part 2, Chapter 17, McGraw-Hill, New York, 1967.

[30] J.A. Thornton, Annu. Rev. Mater. Sci. 7 (1977) 239.

[31] J.A. Thornton, J. Vac. Sci. Technol. 11 (4) (1974) 666.

[32] F.R. Blom, et al., Thin Solid Films 204 (1991) 365.

[33] K.-S. Weibenrieder, J.M. Mueller, Thin Solid Films 300 (1997) 30.

[34] O.S. Heavens, Optical Properties of Thin Solid Films Chapter 4, Dover, New York, 1954, p. 58.

[35] S. Ohtani, Prog. Cryst. Growth Charact. 17 (1988) 171.

[36] M.S. Tomar, F.J. Garcia, Prog. Cryst. Growth Charact. 4 (1981) 221.

[37] H. Demiryont, K.E. Nietering, Sol. Energy Mater. 9 (1989) 79.